Precise Registration of Laser Mapping Data by Planar Feature Extraction for Deformation Monitoring

Arpan Kusari, *Member, IEEE*, Craig L. Glennie, *Member, IEEE*, Benjamin A. Brooks, *Member, IEEE*, and Todd L. Ericksen

***Abstract*— Quantifying near-field displacements can help enable a better understanding of earthquake physics and hazards. To date, established remote sensing techniques have failed to recover subcentimeter-level near-field displacements at the scale and resolution required for shallow fault physical investigations. In this paper, methods are developed to rapidly extract planar parameters, using fast parallel approaches and an alternative registration approach is employed to automatically match the planes extracted from pairwise temporally spaced mobile laser scanning (MLS) and Airborne laser scanning (ALS) data sets along the Napa fault. The features extracted from two temporally spaced point clouds are then used to calculate rigid-body transformation parameters. The production of robust and accurate deformation maps requires the selection of appropriate planar feature extraction and feature mapping criteria. Rigorously propagated point accuracy estimates are employed to produce realistic estimated errors for the transformation parameters. Displacements of each aggregate study area are computed separately from left and right sides of the fault and compared to be within 3 mm of alinement array displacements. Local differential displacements show distinct patterns which, compared to alinement array measurements, were found to agree within the confidence bounds. The findings demonstrate the ability to accurately estimate near-field deformations from repeated MLS or ALS scans of earthquake-prone urban areas. ALS is also used in conjunction with the MLS data sets, illustrating the algorithm's ability to accommodate different LiDAR collection modalities at subcentimeter-level accuracy. The automated planar extraction and registration is an important contribution to the study of near-field earthquake dynamics and can be used as input observations for future geological inversion models.**

***Index Terms*— LiDAR, near field, octree, planes, registration.**

I. Introduction

ACCURATE quantification of surface deformation is essential to understand the general mechanisms of earthquake ruptures, for inferring the nature of fault slip at depth, and for assessing seismic hazards [1]–[5]. However, the surface expression of earthquake ruptures can be quite complex and difficult to map, especially in the near field (<1 km from earthquake rupture) [5]. Various remote sensing techniques have been applied for mapping of earthquake surface deformation; however, to date, these have primarily been restricted to observations in the far field (>1 km from the fault).

High-resolution synthetic aperture radar (SAR) data have been used for mapping ground displacement by calculating the ratio or difference between multitemporal SAR imagery and then using classification strategies [6], [7]. For example, SAR revealed over 2 m of slip at a blind strike-slip fault due to the 2003 Bam, Iran earthquake mapped using ENVISAT radar data [3]. Differential Interferometry (DInSAR) has been used to map far-field deformation of earthquakes by calculating the phase difference between SAR images acquired before and after the earthquake following the work in [5], and it is now so commonly used to study earthquake-related deformation that it has become part of operational post-earthquake analysis products produced by organizations such as the United States Geological Survey [8]. DInSAR is capable of achieving centimeter-level accuracy measuring far-field deformations; however, near the fault, changes in radar scattering properties due to large ground motions often precludes properly unwrapping phase observations and can render the technique ineffective [9]. Global navigation satellite system (GNSS) measurements are also used routinely to estimate 3-D static [10] and dynamic [11] coseismic displacements. These studies have clearly shown that GNSS observations can recover far-field displacements with subcentimeter precision; however, GNSS observations are primarily limited to the far-field because of the high cost of installing and operating a sufficiently dense GNSS network.

Recently, emergent remote sensing techniques, optical imagery correlation, and laser scanning have demonstrated the potential for mapping near-field deformation. For example, the Co-Registration of Optically Sensed Images and Correlation (COSI-Corr) method has been developed by Leprince *et al.* [12] for automatic coregistration of optical imagery without external information such as GNSS measurements of ground control points. COSI-Corr offers advantages over traditional methods of slip because it enables measurements across the entire zone and over wide aperture [13]. It has been used to quantify surface slip measurements for various earthquake studies such as the 1992 Mw 7.3 Landers

Manuscript received July 13, 2018; revised September 9, 2018; accepted November 7, 2018. Date of publication December 20, 2018; date of current version May 28, 2019. This work was supported in part by the United States Geological Survey under Grant G16AC00135 and in part by the National Science Foundation EAR/IF Program under Grant 1339015. *(Corresponding author: Arpan Kusari.)*

A. Kusari was with the Department of Civil and Environmental Engineering, University of Houston, Houston, TX 77204 USA. He is now is with Ford Motor Company, Dearborn, MI 48124 USA (e-mail: akusari@uh.edu).

C. L. Glennie is with the Department of Civil and Environmental Engineering, University of Houston, TX 77204 USA (e-mail: clglenni@central.uh.edu).

B. A. Brooks and T. L. Ericksen are with the United States Geological Survey, Earthquake Science Center, Menlo Park, CA 94025 USA.

Color versions of one or more of the figures in this paper are available online at http://ieeexplore.ieee.org.

Digital Object Identifier 10.1109/TGRS.2018.2884712

earthquake [13] and 2013 Mw 7.7 Balochistan, Pakistan earthquake [14]. Although the method retrieves near-field horizontal movements accurate to the decimeter level, it does not directly provide a complete 3-D displacement field essential for earthquake deformation mapping. In contrast, laser scanning directly measures the 3-D geometry and can provide 3-D displacement field estimates. Airborne laser scanning (ALS) was first used to produce detailed 3-D models of the entire fault zone in [15]. Recent ALS results include [16] where used pre-event and postevent digital elevation models (DEMs) were used to estimate vertical displacements and reveal surface ruptures, and [17]–[19] which used an iterative closest point (ICP) method [20] to register pre-earthquake and post-earthquake ALS scans and derive 3-D seismic displacements. These studies proved that ALS could be used to estimate near-field displacements. However, the accuracy of ALS is limited to decimeter scale and does not capture small movements which may be significant to the mapping and analysis of surface deformation. Finally, temporally spaced terrestrial laser scans have also been used for deformation measurement using least squares 3-D surface matching but they are severely limited by the restricted areal extent of data acquisition [21].

Here, we hypothesize that the high precision of LiDAR observations can be used to provide deformation estimates between consecutive scans in an automated manner and that planar features of man-made structures can be used as control surfaces (persistent scatterers) to be registered in repeat passes of LiDAR surveys to improve the accuracy of the extracted transformation parameters when compared to simple point cloud matching techniques such as ICP. The development of automated methods is paramount for reacting to earthquakes where low latency derived displacement fields are essential. We propose and detail the use of a hierarchical "octree" data structure to partition small subsets of point clouds to permit identification of neighboring points (topology) as a preliminary segmentation step. The planar features must be extracted from the finest octree nodes by realizing best fit planes for the points. Thresholding parameters, specific to different data sets, dictate the choice of planar nodes and region growing operations. A registration approach based on an iterative rigid body least squares solution is then performed to condition the points of planar surfaces to lie on a matched planar surface from temporally distinct point clouds. The common planar features of two consecutive data sets are then matched utilizing some matching criteria. Both global and local displacement estimates are then extracted for the data sets. We compare the global estimates with ground truth observations to determine the accuracy of the approach, while the local spatial varying estimates provide a picture of the ability to resolve localized deformation. A point accuracy (PA) measure based on the error propagation of the hardware components of the laser scanning system and error due to terrain are also implemented to examine if weighting the observations by estimated accuracy causes significant changes to the displacement estimates. The intended area of application is to urban or suburban areas that have multiple built structures and that are prone to surface displacements related to earthquakes [22].

II. Methodology

A parallel segmentation approach using the octree data structure is performed to divide the data set into a hierarchical structure. A least squares best-fit implementation is performed on each leaf node (end node) to extract the planar regions. The planar regions are grouped to form planar features using connected-component labeling (CCL) algorithm. The steps are detailed in the following.

A. Parallel Octree Generation

The data structure implemented for regularizing the anisotropic point data should provide easy access to the nodes as well as the neighbor information for each node but still be developed in real time. With these constraints in mind, a parallel octree implementation is adapted from [23] which capitalizes on the modern GPU's massively parallel architecture accessible in an OpenCL environment. OpenCL specification [24], designed by the Khronos group, is a new industry standard used for general purpose GPU (GPGPU). It has specific advantages over NVIDIAs CUDA including programing for heterogeneous systems of either GPUs and/or CPUs and is supported by various kinds of GPU vendors (NVIDIA, AMD, Apple, Intel, and so on).

The fundamental basis of the parallel octree algorithm is the construction of a tree based on level-order traversals, whereby all the octree nodes at the same level are processed in parallel. The parallel structure of the octree maximizes the number of nodes processed by spawning a new thread for every new node in the same level. Following the normal convention, the voxel containing the entire data set is referred to as the root and the voxels at the finest level are called leaf nodes. The selection of the maximum depth level is made by calculating it from the minimum size of the octree node that is input as a parameter. This allows us to construct data structures based on the variable point spacing of the different LiDAR data collection systems. 64 bits are used to represent the key, increasing the maximum depth level to 20 and employs a much simpler octree data structure than given in [23].

An example pointcloud is given in the Fig. 1(a) and the octree segmentation is given in Fig. 1(b).

B. Planar Least Squares Fit

In 3-D Euclidean space, a plane can be given by a hessian-normal form as

$$ax + by + cz + d = 0 \tag{1}$$

where $\mathbf{n} = (a, b, c)$ is the unit normal vector and d is the distance from the plane to the origin of the coordinate system. For a point cloud, $P = (x_i, y_i, z_i), 1 \leq i \leq N$, the observation equation is given as

$$J(p, n) = \sum_{i=1}^{N} [\mathbf{n} \cdot (p_i - \bar{p})]^2. \tag{2}$$

The centroid of the data set must lie on the least squares plane [25]. The direction of the plane, $\mathbf{n}$, can be solved by constraining the objective function (i.e., the sum of the

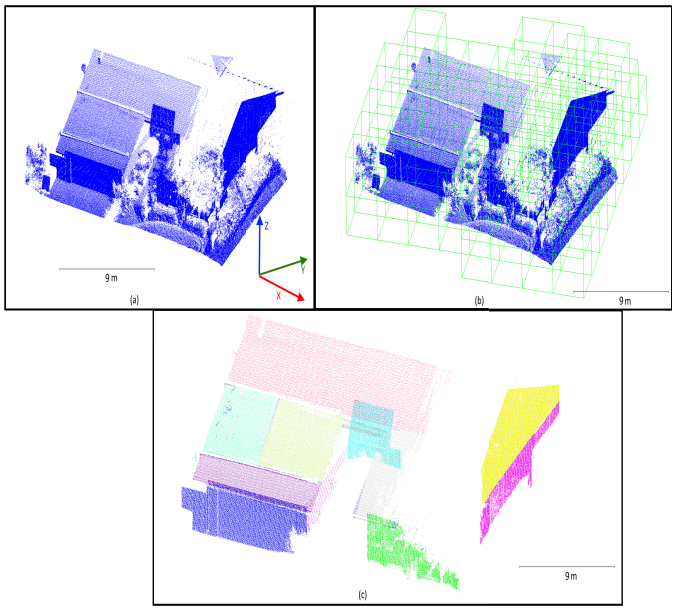

Fig. 1. Segmentation and planar region growing steps. (a) Original point cloud. (b) Octree division of the point cloud (green boxes representing nodes after third level of division). (c) Extracted planar surfaces colorized.

squares of the direction cosines must equal unity) subject to minimization of J, given by

$$G = a^2 + b^2 + c^2 - 1 = 0. \tag{3}$$

For a matrix M containing the data points, the function J is minimized using the Lagrange multiplier (λ). The resulting equations are given by

$$\nabla J = \lambda \nabla G \tag{4}$$

and

$$(M^T M)\mathbf{n} = \lambda \mathbf{n} \tag{5}$$

(known as the normal equations) can then be solved using eigen analysis. $M^T M$ is denoted as the normal (or covariance) matrix C, which is defined as

$$C = \sum_{i=1}^{N} \begin{bmatrix} x_i^2 & x_i \cdot y_i & x_i \cdot z_i \\ x_i \cdot y_i & y_i^2 & y_i \cdot z_i \\ x_i \cdot z_i & y_i \cdot z_i & z_i^2 \end{bmatrix} \tag{6}$$

where x, y and z are the spatial coordinates of a given point p_i.

The problem can also be solved using singular value decomposition of M since the eigenvectors of C are also singular vectors [26]. The solution then is given by the right singular vector corresponding to the smallest singular value.

The planar fit of every octree node is computed in parallel by following the eigenvalue analysis given by (5). The covariance matrices of all the points of the octree nodes are constructed. The covariance matrices are then used to find the smallest eigenvalues which help us compute the corresponding eigenvectors, providing us with the planar normals. The planar normals are used to test if the octree nodes are planes using a limiting criterion. The steps are provided in Algorithm 1.

Algorithm 1 Parallel Least Squares Planar Extraction

Input: points, planar threshold
Output: planar nodes
for each of the nodes in parallel **do**
  N ← number of points in node
  for j=1 to N **do**
    Calculate covariance matrix C
  end for
  find eigen values from C
  find eigenvector of smallest eigenvalue
  for j = 1 to N **do**
    Check if Point within planar threshold
  end for
  if points within threshold greater than threshold **then**
    specify node as plane
  end if
end for

C. Region Growing Using Connected Component Labeling

The region growing method needs to incorporate the planar information of the leaf nodes. A simple solution would be to find the planar information of every leaf node in the octree and then compute the following distance metrics for the neighboring nodes:

$$\text{dist}_{\text{normal}}(p_1, p_2) = \langle \mathbf{n_1} \cdot \mathbf{n_2} \rangle \tag{7}$$

and

$$\text{dist}_{\text{point-plane}}(p_1, p_2) = \langle \mathbf{n_1} \cdot \mathbf{c_2} \rangle + d_2 \tag{8}$$

where $\mathbf{n_1}$ and $\mathbf{n_2}$ are the planar normals of two best fit planes, d_1 is the planar distance of the first best fit plane, and $\mathbf{c_2}$ is the centroid of the second best fit plane. Thresholds are provided for both normal and range distances to detect planar surfaces.

The CCL algorithm is highly parallelizable because the labels can be updated independently of each other. Therefore, an attempt is made to parallelize the algorithm (see Algorithm 2) by modifying the modified 8-directional label selection algorithm given by [27] for checking planar nodes and growing planar regions. The original algorithm performs CCL on an image by checking the minimum label in every direction at every iteration. The algorithm is modified to work for octree nodes by specifying labels for all the planar nodes that are connected and within a threshold. At every iteration, the old label for a planar node is initially assigned to be the minimum label. All 27 neighbors are checked for matching planes and the minimum of those labels are assigned as the minimum label for this node. All directions are continually searched until a nonplanar node is encountered. Iterations are stopped when the labels no longer change. A check is applied at the end of two iterations to find whether the label assigned is the smallest to expedite the region growing process. This is performed by checking whether the label of the ith node is i. If it is, the label is taken to be the smallest and then all the nodes having the label i are excluded from check in the next iteration.

Algorithm 2 Parallel Planar Region Growing Algorithm

```
Input: nodes
Output: labels
for j = 0 to n iterations do
  for each of the nodes in parallel do
    if node i is a plane then
      Assign old label of i as minimum label
      for k = 1 to 27 directions do
        if neighbor nodes are planes and dot product is
          within threshold then
          Compare labels and assign minimum label
        end if
      end for
    end if
  end for
  if j = 2 and label of i is smallest then
    stop comparing i node
  end if
  if no label change then
    exit
  end if
end for
```

Once the labels are determined, the nodes having the same labels are gathered. This is a simple yet time-consuming operation in sequential processing, but fortunately can be performed in parallel as well. The parallel radix sort orders all the labels along with the indices in the original array. Then, a unique label finding operation is performed where the unique labels, the number of nodes having the label, and the first index of the label in the sorted array are output. The results of these operations are the consolidated planar regions in the data set. The final planar regions of the example pointcloud are shown in Fig. 1(c). Further details on the octree generation and CCL operations can be found in [28].

D. Planar Matching and Registration

In the case of urban/suburban areas, planar surfaces are present in abundance and, thus, can be exploited to strengthen the least square estimation of differences between temporally spaced point clouds. The correspondences between the before (t−1) and after (t) planar patches need to be established in order to define a rigid transformation. An assumption is made that the postevent planes have undergone minuscule rotation (within 1°) in all three axes due to earthquake movement, which is justified by the results presented in [17]. This assumption is valid for all georeferenced point clouds using the same geodetic datum and simplifies the search for correspondence. For every plane in the t−1 point cloud, a search is performed to find the nearest planar surface with a similar surface normal and plane-centroid distance below a certain threshold in the time t point cloud. If such a plane is found, then the planes are said to be matched and can be used in registration.

For two LiDAR point clouds, X_I and X_F, with an unknown spatial difference between them, a rigid body transformation can be defined to align the point clouds as

$$X_F = R \cdot X_I + t_l \tag{9}$$

where R is the rotation matrix and t_l is the translation. The rotation matrix can be simplified using the approximations $\sin\theta = \theta$ and $\cos\theta = 1$, if small-angle rotations are assumed, and thus transforms the nonlinear rotation matrix into the linear form

$$R = \begin{bmatrix} 1 & -\gamma & \beta \\ \gamma & 1 & -\alpha \\ -\beta & \alpha & 1 \end{bmatrix}$$

where α, β, and γ are the rotation angles about the three orthogonal axes, and the translation is given as $t_l = (t_x, t_y, t_z)^T$. A least squares approach detailed in [29] uses planar constraints to determine airborne LiDAR system boresight parameters. This constrained planar solution is modified to extract optimized rigid body transformation parameters by conditioning the geo-referenced LiDAR target points to lie on planes. The functional model for a point j with coordinates $P_j = [x_j, y_j, z_j]$, lying on plane i, is given as

$$\left\langle \overrightarrow{p_i}, \begin{bmatrix} \overrightarrow{P_j} \\ 1 \end{bmatrix} \right\rangle = 0 = f(\overrightarrow{l}, \overrightarrow{x_1}, \overrightarrow{x_2}) = f\left(\overrightarrow{l}^{\,\mathrm{obs}} + \hat{v}, \overrightarrow{x_1}^0 + \hat{\delta_1}, \overrightarrow{x_2}^0 + \hat{\delta_2}\right) \tag{10}$$

where the position vector of observed point j on the plane $\overrightarrow{P_j} = h(\overrightarrow{l_i}, \overrightarrow{x_1})$ is a function of the LiDAR observations $\overrightarrow{l_i} = [X\ Y\ Z]_i^T$; the calibration parameters are $\overrightarrow{x_1} = [\alpha\ \beta\ \gamma\ t_x\ t_y\ t_z]$; $\overrightarrow{x_2}$ are the vector of plane parameters; δ_1 and δ_2 are the estimated corrections to calibration and plane parameters and $\hat{v}$ are the observational residuals.

Expanding (9) and substituting into (10) leads to the functional form of

$$\left\langle \overrightarrow{p_i}, \begin{bmatrix} R \begin{bmatrix} x_j \\ y_j \\ z_j \end{bmatrix} + \begin{bmatrix} t_x \\ t_y \\ t_z \end{bmatrix} \\ 1 \end{bmatrix} \right\rangle = 0. \tag{11}$$

For a points and b planes, $a \gg b$, there are a conditions, $n = 3a$ observations and $u = 6 + 4b$ unknowns. For every plane, a unit length constraint needs to be satisfied, and therefore, the number of constraints is b.

Solving this iterative least squares problem (Appendix) gives us the transformation parameters between the data sets. Therefore, for pre-event and postevent data sets, this iterative solution delivers the estimated displacement due to the earthquake. In order to determine the relative movement between the left and right sides of the fault, the displacements are computed separately and differenced.

E. Point Accuracy Estimation

The quantification of the PA in three dimensions is central to the point-to-plane registration algorithm because the displacement estimation requires an estimate of PA (weight matrix P). The preliminary stochastic model considers all observational errors to be uncorrelated and zero mean. This assumption provides a case where considering a purely diagonal covariance

matrix allows a simplified model for efficient processing of large data sets. Considering this, the weight matrix, P for the observations, is assumed to be diagonal given by

$$P = \begin{bmatrix} P_x & 0 & 0 \\ 0 & P_y & 0 \\ 0 & 0 & P_z \end{bmatrix} \tag{12}$$

with $P_i = (1/\sigma_i^2)$ where σ_i is the point uncertainty in the ith direction.

For the initial analysis, all coordinates are weighed equally. This assumption is not justified since the errors of the laser scanner components affect the PA in each dimension differently. Therefore, for rigorous estimation of displacement accuracy estimates, the PA for each LiDAR point can be estimated by propagating the error from the laser scanner components and including the error due to uncertainty induced by terrain. More realistic weighting should also provide properly scaled estimates of uncertainty of the surface deformations.

There are numerous factors affecting the accuracy of the final coordinates, which have been extensively studied [30]. For our error analysis, only stochastic error sources are taken into account. The point uncertainty is estimated in two steps.

1) *Error Propagation Through LiDAR Georeferencing Equation:* The ground coordinates for scan-points in a point cloud are calculated using the georeferencing equation [31] by combining the information from the scanner, the integrated GNSS/Inertial Navigation System measurements and calibration parameters. The georeferencing equation is nonlinear and the individual effects of the errors of the sources can be calculated by linearizing using Taylor series expansion and truncating after the first term. The nominal PA is then given by using Special Law of Propagation of Variance formula. For details, the reader is referred to [31].
2) *Error Due to Surface Morphology:* While the error propagation estimates the error due to instrumentation, the error induced by the process of interaction of the laser pulse with the surface needs to be quantified, which can introduce additional uncertainty in the actual position of the laser point. Bray *et al.* [32] model the laser beam as a cone with the footprint of the beam being modeled assumed to be an ellipse formed by the intersection of the cone and the local plane estimated from the nearest neighbors. The 2-D ellipse gives us the covariance information in the direction of the normal which is then rotated to Universal Transverse Mercator coordinate framework to output the full 3-D error due to incidence. The total error is given by

$$C_{\text{total}} = C_{\text{nominal}} + C_{\text{surface}} \tag{13}$$

adding the nominal covariance and covariance due to surface morphology.

III. Study Area

In this paper, we use two mobile laser scanning (MLS) data sets and three ALS data sets from a study area surrounding the Napa fault, to examine the ability of the proposed planar technique for estimating the near-field displacements. The West Napa Fault is a geological right lateral strike-slip fault located in Napa County, California, and was the source of the Mw 6.0 earthquake on August 24, 2014. The earthquake was the first major earthquake in the San Francisco Bay Area since 1989 and was the cause of $1 billion in monetary damages and a life lost. Hand measurements made immediately following the earthquake documented 5–50 cm of slip in the northern section of the fault, and consistently less than 5 cm of coseismic slip in the southern section. However, immediately following the earthquake (within 3 h) afterslip was detected by alinement array stations on the southern half of the fault, and accumulated tens of centimeters of displacement [33]–[35]. MLS observations were made along approximately 85% of the fault on September 1 and 2, 2014, and to document afterslip, an additional set of MLS observations was collected on September 28–30th, 2014. An overview of the fault and the MLS platform coverage is given in Fig. 2. For our analysis, we have examined two distinct areas along the Napa fault: the northern section which was subjected to little afterslip, and the southern section where significant afterslip was detected by alinement stations. The northern study area is a suburban neighborhood called Browns Valley that contains a large number of residential structures. The southern area is nearer to the epicenter of the earthquake and the coseismic displacements in this area were much smaller than the Browns Valley area—on the order of 5–6 cm [36]. Brooks *et al.* [37] showed the photographs taken at the same location in and around the area having a large amount of afterslip (20 cm) within the first 24 h following the earthquake. Since then, the afterslip has decayed considerably but is still predicted to be 30 cm over a 2–3-year period [11]. This region, shown in the lower black box in Fig. 2, consists of mostly ranch houses and has two alinement array stations, labeled as NLAR and NWIT. This is a rural region, and therefore, buildings are sparse. The sparse planar features help to test the robustness of our algorithm for determining realistic offsets with minimal observational redundancy.

In order to establish the flexibility of the algorithm in dealing with different kinds of scanning systems, three different ALS data sets (two pre-event and one postevent) are used to derive the displacements among themselves and in combination with the MLS data sets. The first prevent ALS data set was acquired by National Center for Airborne Laser Mapping for the Napa River Watershed survey during May 15 to June 1, 2003, covering an area of 1500 km^2 with a point density of 1.45 points/m^2. The second, more recent pre-event ALS data set was acquired by Quantum Spatial on June 7, 2014 for an update of base maps for the city of Napa. The data set was acquired using a Leica ALS60 scanner with a point density of 10 points/m^2. The postevent ALS data set was acquired by Towill, Inc., using an Optech Orion M300 scanner on September 9, 2014. Although the area extents were similar to the preevent acquisition, the point density was close to 10 points/m^2. The ALS data sets are shown in Fig. 3. Table I summarizes all the ALS and MLS data sets acquired in the Napa region.

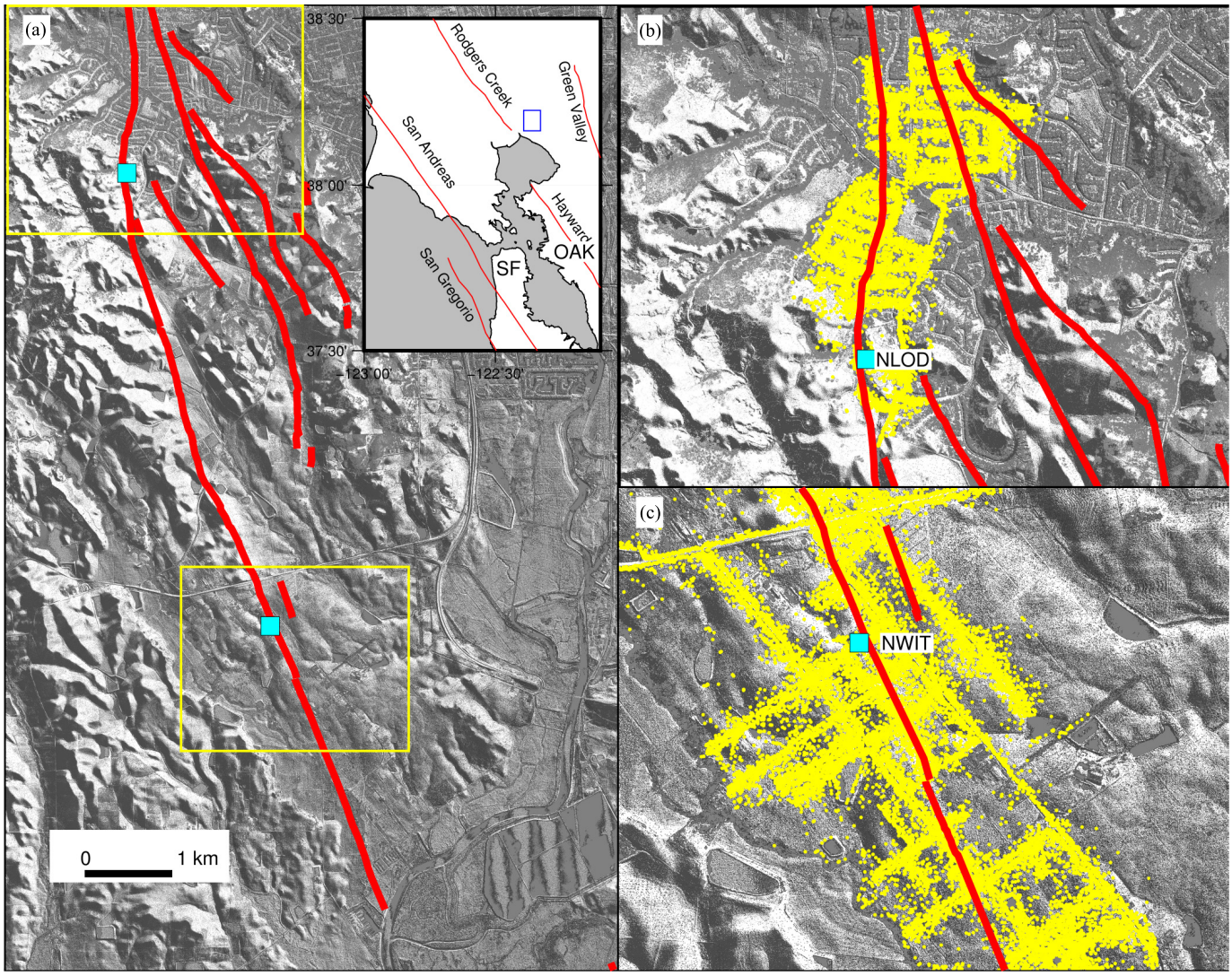

Fig. 2. (Left) Overview of the Napa fault zone with the fault trace in red, alinement array stations in cyan, and the scanned areas in yellow boxes. (Top right) Browns Valley (top yellow box). (Bottom right) South rural Napa. Inset: zoomed-out-image of the scanned area with the different fault traces. Background of image is the ALS DEM hillshade (grayscale).

TABLE I
DESCRIPTION OF ALS AND MLS DATA SETS ENCOMPASSING NAPA REGION

Platform type	Scanner type	Date of acquisition	Area of acquisition	Point density $[pts/m^2]$	Height above ground [m]
ALS	Optech 2033 ALTM	May 15th-June 1st, 2003	Napa county	1.3	700
ALS	Leica ALS60	June 8th, 2014	Napa county	8	900
MLS	Riegl VZ-400	September 1st, 2014	South Rural Napa	275.3	-
MLS	Riegl VZ-400	September 2nd, 2014	Browns Valley	284.1	-
ALS	Optech Orion M300	September 9th, 2014	Napa earthquake	11.4	750
MLS	Riegl VZ-400	September 28-29th, 2014	South Rural Napa	274.1	-
MLS	Riegl VZ-400	September 30th, 2014	Browns Valley	282.9	-

IV. RESULTS

A. Browns Valley MLS Displacements (Napa Fault)

For suburban Browns Valley, two MLS data sets were collected on September 2, 2014 and September 30, 2014 to measure afterslip. Alinement arrays were set up along the main fault line trace of the Napa earthquake [38] and were periodically observed to measure afterslip, with estimated accuracy better than 1 mm. The alinement array site closest to the Browns Valley area was NLOD and, therefore, served as the primary reference for the MLS estimates of afterslip. For estimating horizontal displacements, we were primarily interested in examining the above-mentioned ground planar features (i.e., buildings). Therefore, the first processing step for all MLS scans was to remove the ground points by filtering. Ground planes in this region are mostly horizontal and, therefore, offer little or poor constraints on the expected dominant horizontal afterslip motion of the Napa fault.

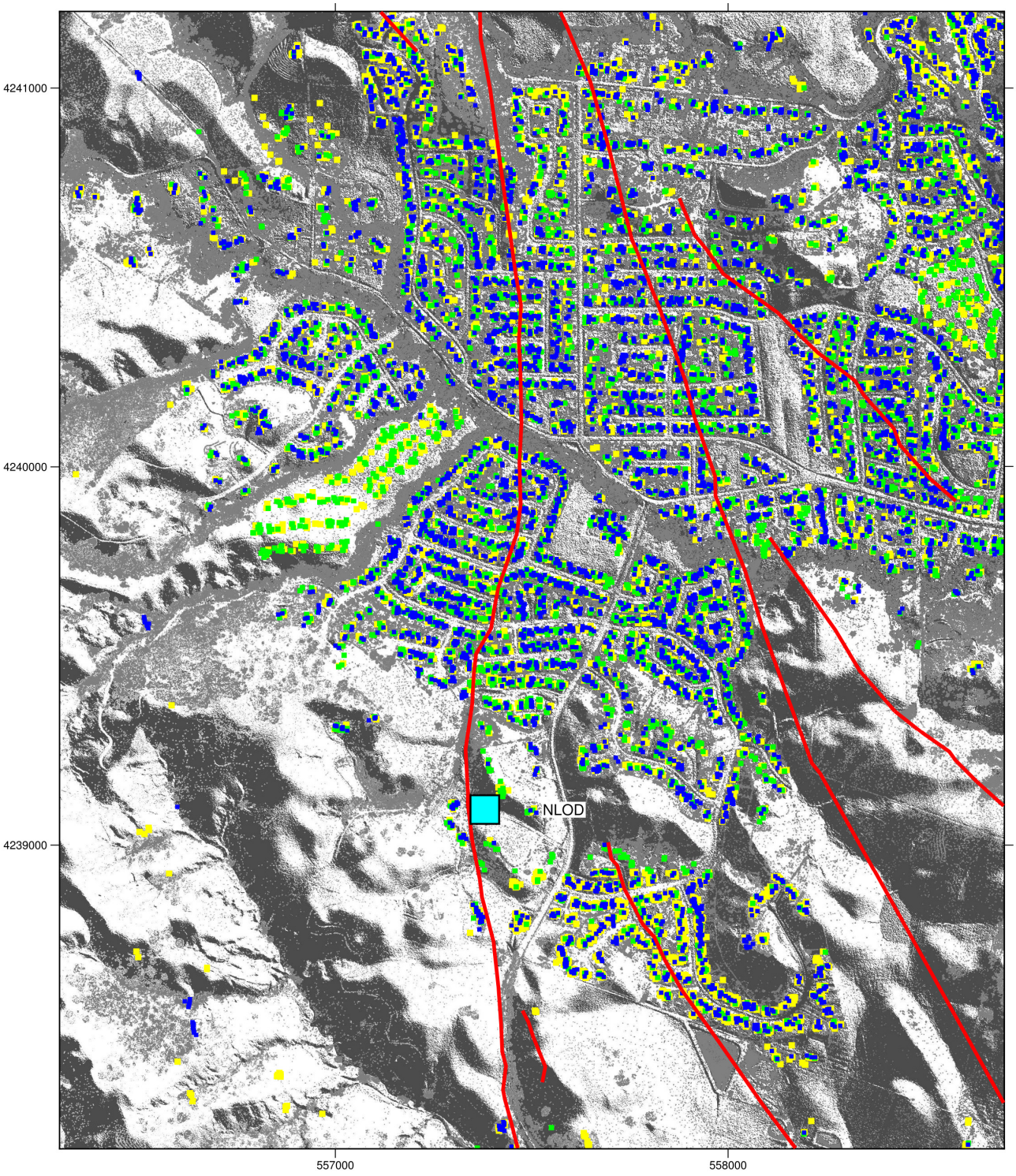

Fig. 3. Overview of the extracted rooftops from ALS data sets for the Napa fault. Blue: 2003 data set. Green: June 2014 data set. Yellow: September 2014 data set. Red: fault trace. Cyan: alinement array.

Several algorithms have been proposed to filter ground points for ALS data sets [39]. The ground points filtering algorithm provided in the commercial software, Terrascan was used which starts from a sparse triangulated irregular network and is iteratively refined the ground definition using the laser point set based on user-specified thresholds [40]. After the automated filtering, some limited manual exclusion of points was also applied to clean up the data sets. Planar surfaces were again extracted from the left and the right sides of the fault trace with a 10 m buffer around the *a priori* known fault trace location.

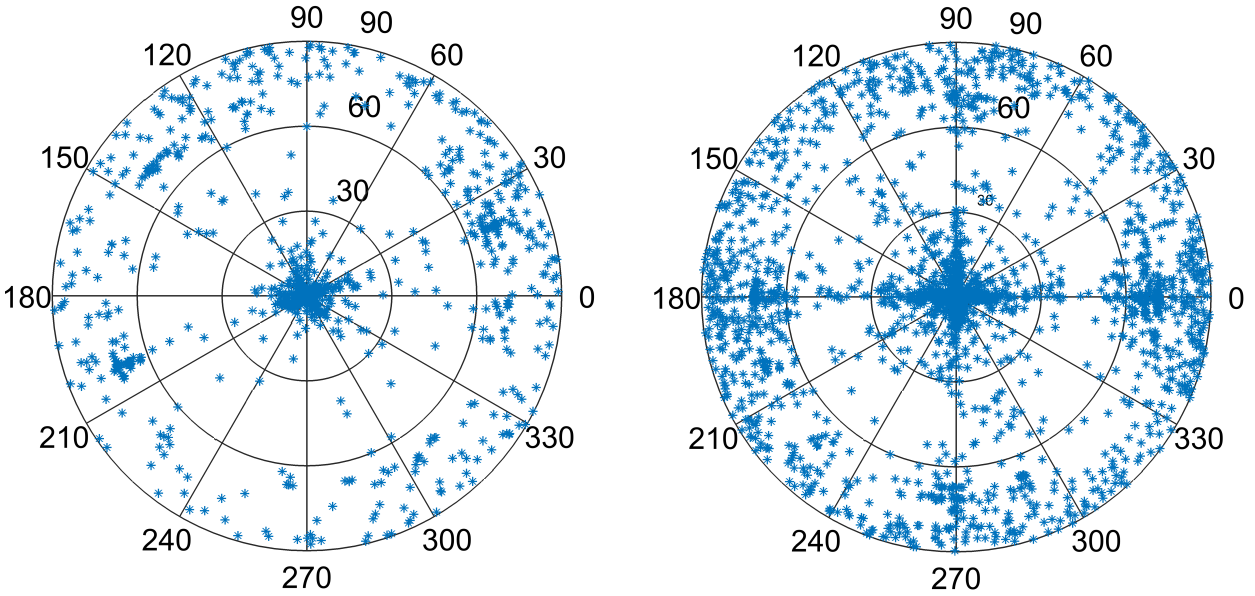

Fig. 4. Polar plots of azimuth angle versus elevation angle of the normal vector of matched planes used in the estimation of displacement for (a) left and (b) right sides of the Napa fault (Browns Valley) MLS data sets.

The planar surfaces extracted were then used to perform a global registration between the two temporally spaced data sets.

The large point clouds are broken down into tiles to facilitate parallel computation and the displacements are calculated over the tiles. The global displacements are an average of tiles of a certain side of the fault. The initial analysis was performed using a tile size of 20 m but increased tile sizes of 35 and 50 m were also evaluated to determine the effect of tile size on the number of planes and resultant displacement estimates. The number of planes extracted was found to decrease with increasing tile size. This was to be expected as the minimum node size increases, and thus, certain planar surfaces are under segmented or are clustered with vegetation leading to their rejection. Fig. 4 is a polar plot of the normal vector orientation for each matched plane pair and provides a measure of the planar strength in each direction for estimating displacements for left and right sides of the fault. This shows that the solution has observation strength in all particular directions. Note that this is the case for all the Browns Valley comparisons presented here in this paper, and therefore, polar plots for other solution sets are not given. The estimates of afterslip are given in Table II along with the number of planes used to estimate each offset. To estimate afterslip from the alinement array observations, the graph provided in [11] is used. It provides the accumulated slip for the alinement array stations both measured and predicted using the AFTER program [41]. The AFTER function describes the alinement array observations of postseismic slip. The function consists of two terms which characterize the power law, the time dependence, τ, and the temporal index, p. Its chief characteristic is that once time (t) $> \tau$, the deformation nearly ceases.

The accumulated slip was interpolated over the MLS observational period to find the horizontal displacement (Hz) for the NLOD station. This measurement is given along the fault rupture trace and the results show that the MLS fault parallel estimates are slightly smaller than that predicted by the alinement array/AFTER program estimates. This slightly larger disagreement can be attributed to both the fact that the NLOD station is outside the Browns Valley study area and that the alinement array offset was not actually a measured value, but that predicted by the AFTER model. However, the disagreement is close to the combined expected accuracy of the MLS and the alinement array estimates of displacement.

In order to examine spatially varying estimates of afterslip, the left and right sides of the fault were divided into strips of both 100 and 50 m sizes laterally (i.e., perpendicular to the fault), to examine the spatial resolution of the method. Unfortunately, since most of the MLS data were collected on the east side of the fault (see Fig. 2), the majority of the strips west of the fault had an insufficient number of planes to reliably estimate a left-side offset. However, because this is a right lateral strike-slip fault, the movement is only expected on the right-hand side. Therefore, all the planes on the left side were used to calculate a global offset which was then subtracted from each of the right side strip displacement estimates. Fig. 5 shows the fault parallel displacements with respect to the profile distance from north to south and provides a comparison to the global results from the NLOD observations and the AFTER software. The 100-m fault parallel displacements gave more precise estimates than the 50-m displacements due to the increased number of planes used in estimating the displacements. No discernible pattern was evident. All local variations were within the estimated uncertainty of the calculated displacements.

It has been established that local heterogeneous displacements are important to understand the variable near-field deformation and to derive an estimate of spatial resolution achievable [17]. In order to find out if local spatially varying displacements could be derived, point residuals from the least

TABLE II

COMPARISON OF HORIZONTAL FAULT-PARALLEL AFTERSLIP ESTIMATE TO NLOD ALINEMENT ARRAY STATION ESTIMATE USING DIFFERENT TILE SIZES FOR NAPA FAULT AT BROWNS VALLEY NEIGHBORHOOD

Displacements	20 m tiles	35 m tiles	50 m tiles
ΔX (in m)	-0.0059 $\pm$ 0.0029	-0.0064 $\pm$ 0.0024	-0.0085 $\pm$ 0.0021
ΔY (in m)	-0.0169 $\pm$ 0.0054	-0.0167$\pm$ 0.0057	-0.0163 $\pm$ 0.0055
ΔZ (in m)	0.0203$\pm$ 0.0024	0.0186$\pm$ 0.0032	0.0143$\pm$ 0.0057
ΔHz (in m)	0.0179 $\pm$ 0.0062	0.0179 $\pm$ 0.0061	0.0184 $\pm$ 0.0058
ΔHz (fault par) (in m)	0.0166 $\pm$ 0.0057	0.0166 $\pm$ 0.0056	0.0178 $\pm$ 0.0053
ΔHz (NLOD) (in m)	0.0181	0.0181	0.0181
Runtime (in min)	14.5	19.1	23.7
# planes(left\right)	546\1274	521\1236	513\1231

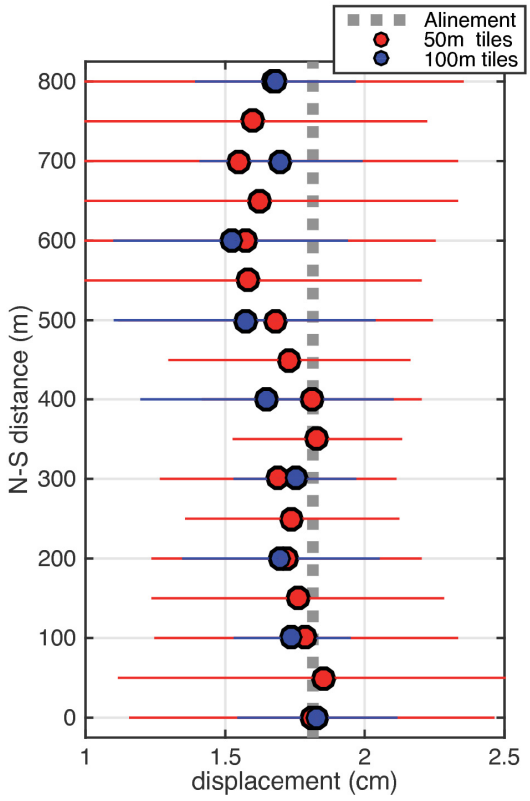

Fig. 5. Fault-parallel horizontal displacements along with estimated accuracies for lateral 50- (red circle) and 100-m (blue square) strips with profile AB (distance increasing from north to south) (Fig. 2). Ground truth measurements are presented for NLOD alinement array estimates (gray dotted line). Error bars represent displacement accuracy estimates at 1 σ.

squares solution are plotted for 50-m tile sizes for the left and right side separately in Fig. 6(a) along with the histograms to show the distribution of the residuals. The residuals could be scaled by (or projected onto) the direction cosines of the planar surfaces on which the individual points lay. Fig. 6(b)–(d) shows the residual components in x-, y-, and y-directions, respectively. To further study whether the residuals exhibit a spatial pattern, a polar plot was given for the mean of the residuals of each plane versus the azimuth angle of the planar normal [Fig. 6(e) and (f)]. The residuals showed no discernible spatial pattern, which suggested that the afterslip from September 2 to September 30 was uniform at the noise level of the method, and therefore, localized displacement analysis was not performed for these data sets.

TABLE III

COMPARISON OF HORIZONTAL FAULT-PARALLEL AFTERSLIP ESTIMATE TO NLOD ALINEMENT ARRAY STATION ESTIMATE WITHOUT PA ESTIMATES AND USING PA ESTIMATES FOR NAPA FAULT AT THE BROWNS VALLEY NEIGHBORHOOD

Displacements	Constant accuracy	Calculated accuracy
ΔX (in m)	-0.0059 $\pm$ 0.0029	-0.0034 $\pm$ 0.0011
ΔY (in m)	-0.0169 $\pm$ 0.0054	-0.0185 $\pm$ 0.0013
ΔZ (in m)	0.0203 $\pm$ 0.0024	0.0025 $\pm$ 0.0009
ΔHz (in m)	0.0179 $\pm$ 0.0062	0.0188 $\pm$ 0.0017
ΔHz (fault par) (in m)	0.0166 $\pm$ 0.0057	0.0182 $\pm$ 0.0015
ΔHz (NLOD) (in m)	0.0181	0.0181
Runtime (in min)	14.5	89.3

1) Point Accuracy Estimates for MLS Displacements: The estimates in Section IV-A assumed a constant PA of 0.05 m for all MLS points in x-, y-, and z-directions, respectively. This accuracy value was based on previous experience evaluating the MLS data from this system. However, point accuracies could vary considerably due to a variety of environmental factors such as heading changes and the incidence angle of the laser on the planar surfaces [31]. Therefore, a PA estimation was performed for the Browns Valley data set. Fig. 7(a)–(c) showed the spatial variation in PA in the x-, y-, and z-directions. The range of the point accuracies in all three directions showed that even though a constant PA measure was reasonable, it did not effectively capture the variability in point uncertainty.

The displacement estimates were then recalculated using actual PA estimates (see Table III). The X displacement was smaller than the X displacement for constant PA while the corresponding Y displacement was larger. The Z displacement was much smaller using the estimated point accuracies, which was expected since for a right lateral strike-slip fault, the vertical displacement was usually small. The fault parallel horizontal displacement showed better agreement with the measured NLOD estimate while the estimated displacement accuracy increased almost by a factor of 2. The inclusion of the realistic PA improved both the accuracy and reliability of the method.

B. Browns Valley ALS Results

Three ALS data sets were captured before and after the Napa earthquake. To investigate the robustness of our planar algorithm, we also attempted to use these temporally spaced ALS observations to estimate the deformations. The data sets were first classified using the Terrascan software and only points belonging to building surfaces were used as inputs for the algorithm. These different ALS data sets were captured

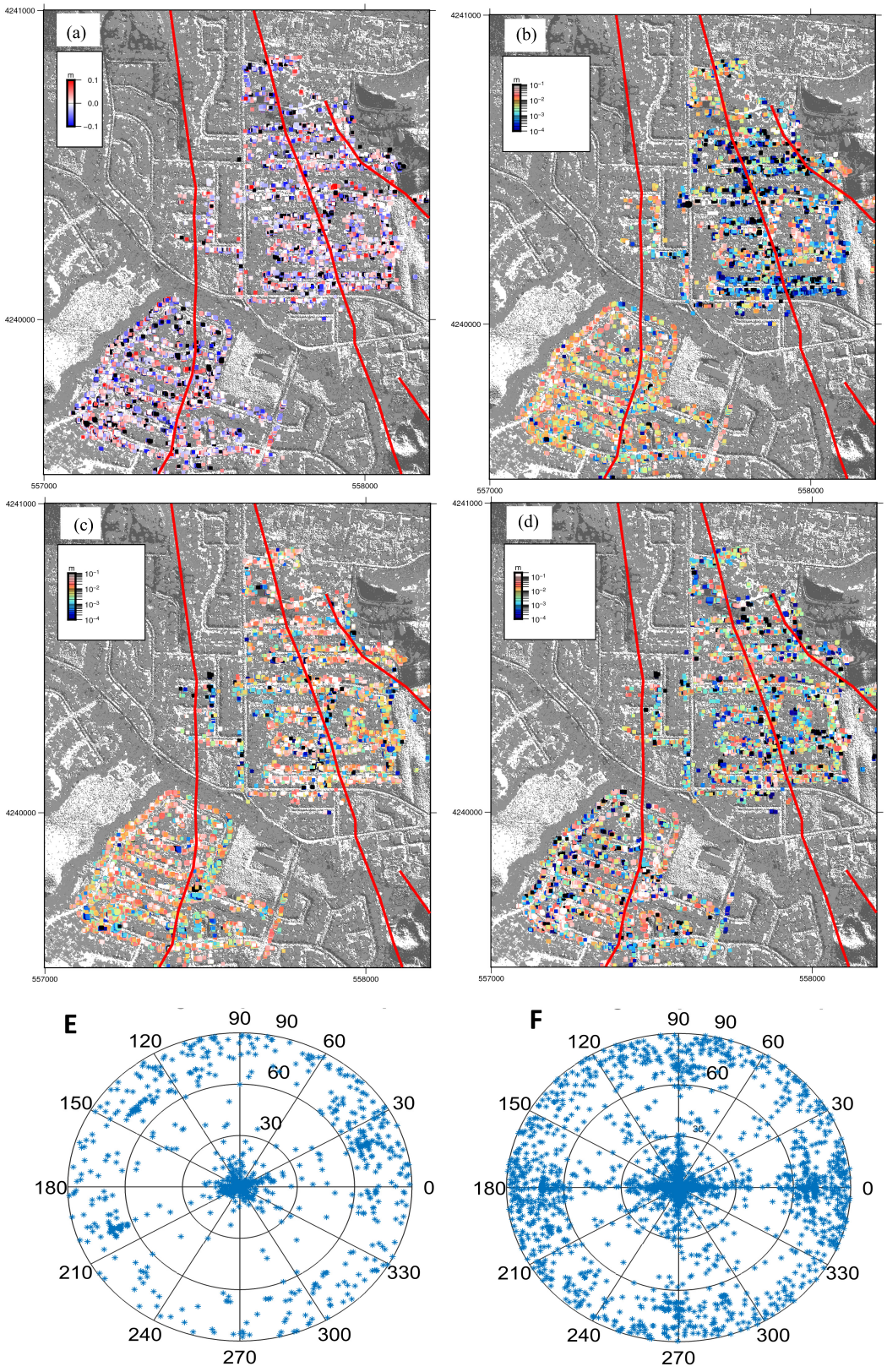

Fig. 6. Least squares residuals of the MLS data set for left and right sides, respectively, for 50-m tile sizes. (a) Residual magnitudes with histograms. (b) X residual component. (c) Y residual component. (d) Z residual component. (e) Polar plot of mean of residuals (in meters) versus azimuth angle of plane (in degrees) for MLS data set left of fault trace. (f) Polar plot of mean of residuals (in meters) versus azimuth angle of plane (in degrees) for MLS data set right of fault trace.

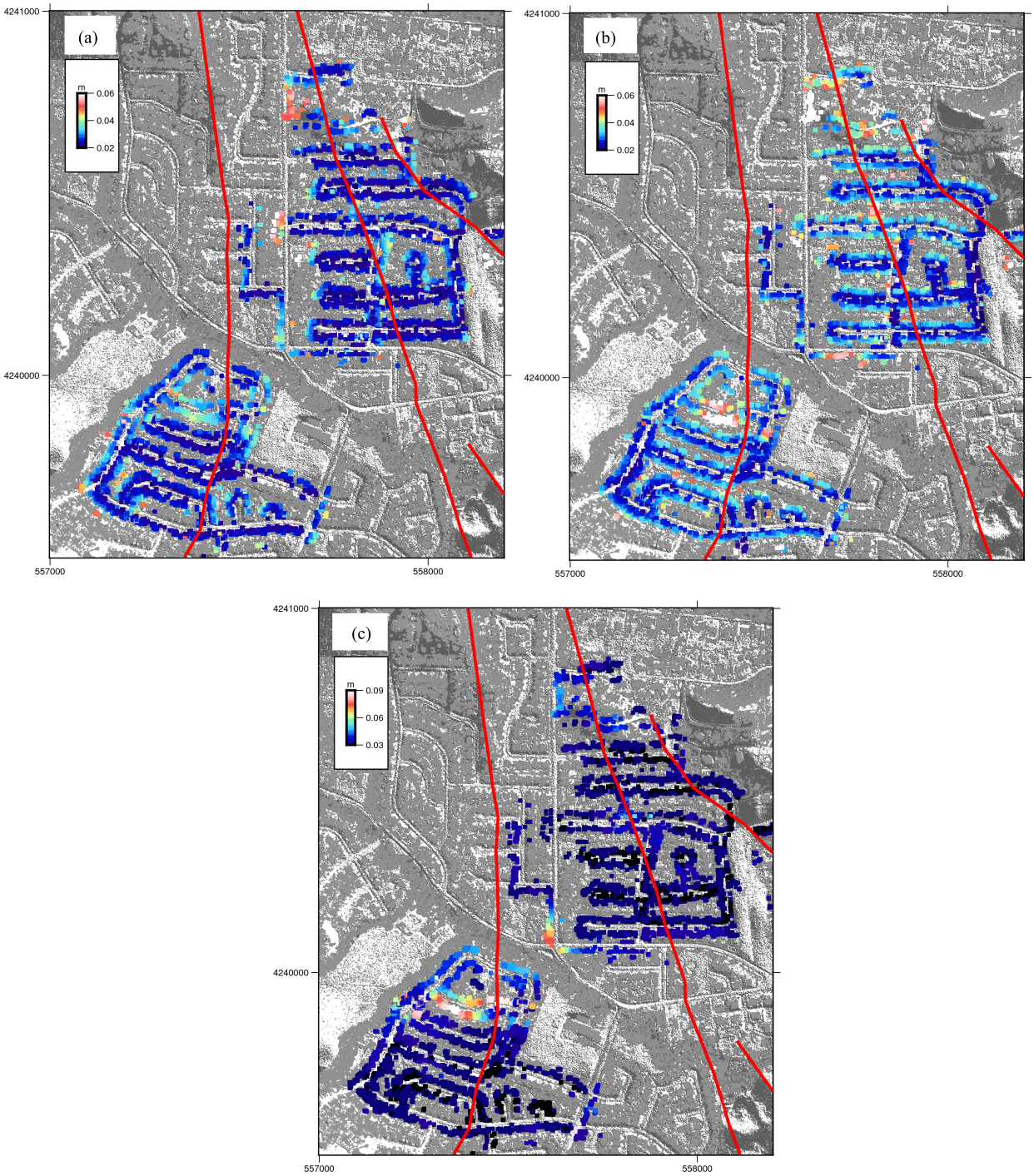

Fig. 7. Estimated PA for (a) X-component, (b) Y-component, and (c) Z-component of the matched planar points for the Browns Valley data set using the Schaer method [32].

in different acquisition conditions, and with different point density which needs to be accounted for in the algorithm. Also, the noise level of the points in the earlier data set (2003) is higher than the later data sets (June 2014 and September 2014). For the first analysis, planar surfaces from the 2003 data set were used in conjunction with the points from the June 2014 data set. The movement between the 2003 data set and the June 2014 data set were given in Table IV. The movement along the fault should be negligible as both the data sets were pre-earthquake but the horizontal fault-parallel estimates were nonzero. This could be attributed to the sparsity of points in the pre-event data set which can give rise to unrealistic Y displacement estimates. Another factor could be an anthropogenic change in structures over the 11-year time span. The estimated displacement accuracy was reported at the centimeter level which was realistic for the noise level of the

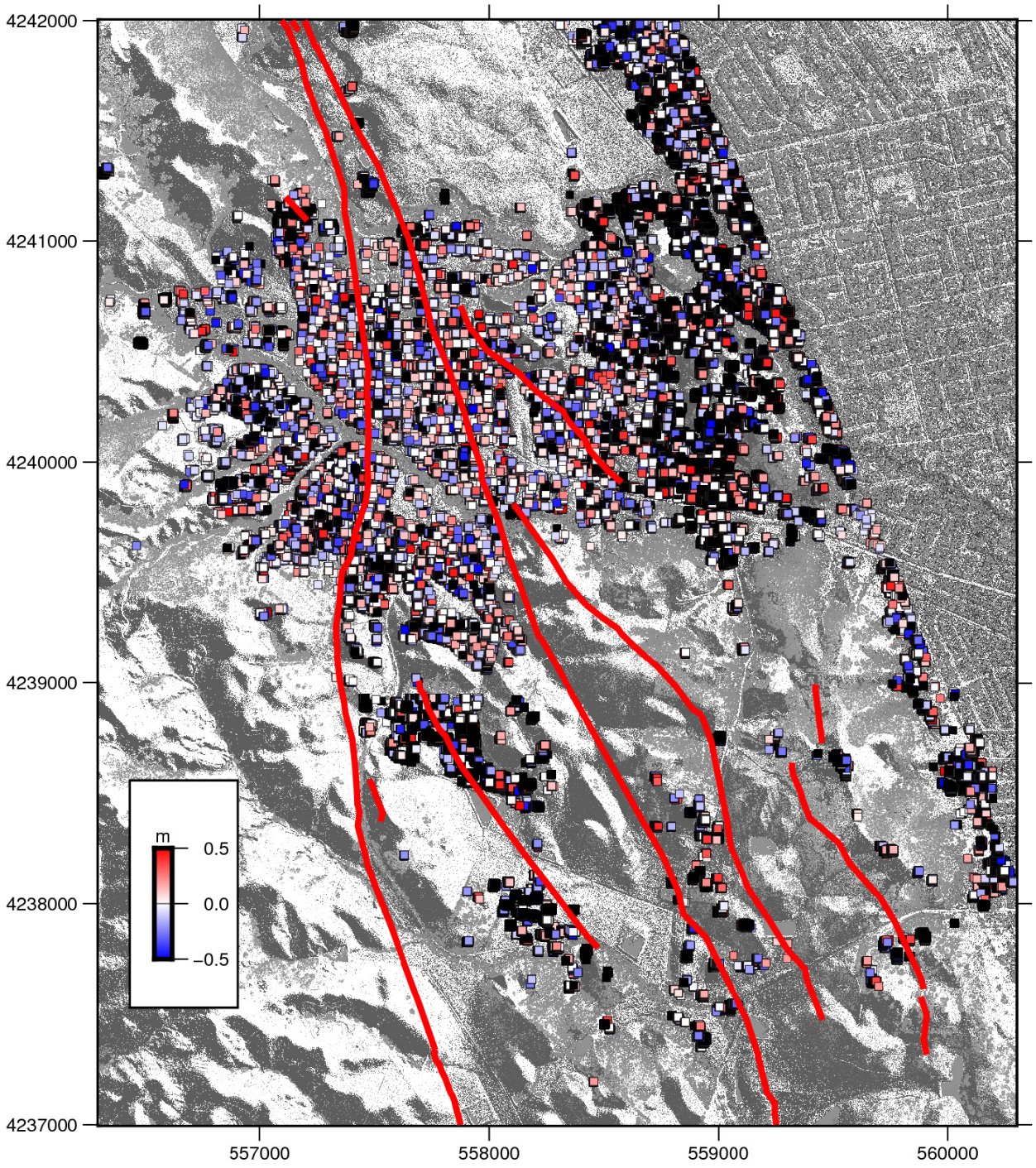

Fig. 8. Signed residual magnitudes for ALS differences (September 2014–June 2014) using 100-m tile sizes with histograms. Solid line: fault lines.

ALS point coordinates and made the estimated Hz statistically insignificant. However, since only the creep motion less than a centimeter was expected [37], the result gave a very good indication of the expected accuracy with which we could determine displacements using ALS.

Between the June 2014 and September 2014 data sets, the shift given by the displacement estimation algorithm should correspond to the combined coseismic and the postseismic displacements (up to September 9, 2014) caused by the 2014 earthquake. The estimated displacements were given in Table V. When compared to the estimated coseismic and postseismic displacements provided by the AFTER program in [11], the ALS displacement seemed to slightly overestimate the motion. The displacement accuracy was better than the corresponding displacement accuracy for the previous ALS–ALS computation which could be attributed to the increased ALS precision and decreased anthropogenic change for the data sets. Overall, the overestimation was well within the expected accuracy of the computed ALS displacement.

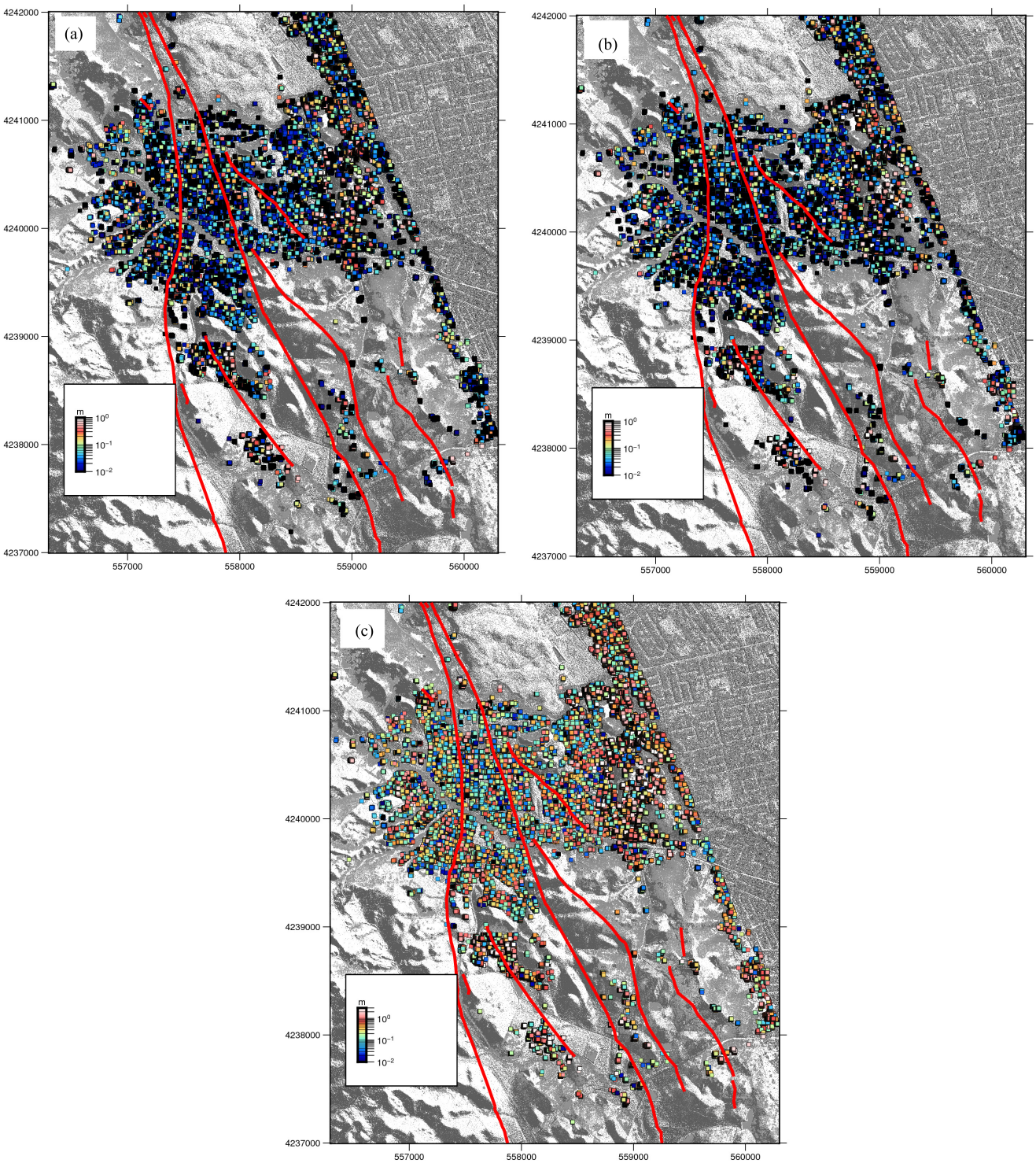

Fig. 9. Estimated ALS data set residual (unsigned) for (a) X-component, (b) Y-component, (c) Z-component using 100-m tiles. Solid line: fault lines. ALS DEM hillshade (grayscale) is provided in background.

A global residual analysis, similar to that performed for the MLS data sets, was attempted for the left and right sides of the fault as shown in Fig. 8 for a 100-m tile size for the June 2014 data set versus September 2014 data set. The residuals were shown as signed variables and fit using a Gaussian distribution for the left and right sides of the fault separately. In order to show a smoothed out difference, a moving window technique was applied to compute localized differences and shift by a small distance in both x- and y-directions (20 m in this case). The histograms did not reveal much information regarding the spatial distribution of the residuals. Since there was not much variability expected for the

TABLE IV

HORIZONTAL FAULT-PARALLEL ALS ESTIMATE FOR JUNE 2003–JUNE 2014 FOR NAPA FAULT AT BROWNS VALLEY NEIGHBORHOOD

Displacements	All tiles (100 m)
ΔX (in m)	0.0011 ± 0.0146
ΔY (in m)	-0.0175 ± 0.0171
ΔZ (in m)	0.00421 ± 0.0098
ΔHz (in m)	0.0178 ± 0.0224
ΔHz (fault par) (in m)	0.0165 ± 0.0207
Runtime (in min)	4.6
# planes(left\right)	819\3712

TABLE V

COMPARISON OF HORIZONTAL FAULT-PARALLEL ALS DISPLACEMENT ESTIMATE TO NLOD ALINEMENT ARRAY STATION ESTIMATE FOR JUNE 2014–SEPTEMBER 2014 FOR NAPA FAULT IN THE BROWNS VALLEY NEIGHBORHOOD

Displacements	All tiles (100 m)
ΔX (in m)	0.0352 ± 0.0134
ΔY (in m)	-0.3153 ± 0.01594
ΔZ (in m)	0.0042 ± 0.0078
ΔHz (in m)	0.3176 ± 0.0208
ΔHz (fault par) (in m)	0.3135 ± 0.0192
ΔHz (NLOD) (in m)	0.3094
Runtime (in min)	4.6
# planes(left\right)	1474\4463

left side of the fault, the residuals of the right side of the fault were then projected onto the planar normals [Fig. 9(a)–(c)]. Inspection of the individual residual components revealed distinct patterns in both the X and Y residual components, especially in the extreme right of the figure which showed complex patterns whereby a simplistic overall displacement appears to mask localized distributions. This suggested that estimation of spatially finer resolution displacements might be possible.

To further investigate if localized patterns could be retrieved from the ALS data sets, the mean of residuals for each plane was plotted with respect to the azimuth angle of the plane in polar plots for 100-, 200-, and 400-m tiles. While 100- and 200-m tile did not show any obvious clusters, the 400-m plot did (Fig. 10). The points from these clusters could be plotted spatially to reveal localized displacement patterns. Fig. 11(a) shows the clusters mapped spatially with diametrically opposite clusters colored the same. It is thus shown that the localized displacements might be recoverable using 400-m blocks but 200-m blocks did not have enough planar features to provide meaningful estimates. Fig. 11(b) and (c) shows the localized displacement estimates for 400-m blocks using a moving window of 20 m for X and Y displacements. The tiled Y displacement estimates appear to show significant localized deformations.

1) Browns Valley ALS–MLS Results: ALS and MLS data sets have different look angles, point densities, and point accuracies. However, there are overlapping planar surfaces between ALS and MLS which could be exploited to provide displacement estimates. The use of combined ALS and MLS data sets is because earthquake-prone zones such as the San Andreas fault have been previously mapped using ALS [42]. Use of MLS for mapping postevent deformation might be a viable method for rapidly and cost effectively estimating displacements in cases where pre-event ALS is available.

TABLE VI

COMPARISON OF HORIZONTAL FAULT-PARALLEL ALS-MLS ESTIMATE TO NLOD ALINEMENT ARRAY STATION ESTIMATE FOR JUNE 2014 ALS–SEPTEMBER 2, 2014 MLS FOR NAPA FAULT AT BROWNS VALLEY NEIGHBORHOOD WITH CONSTANT PA ESTIMATES AND TOTAL PA ESTIMATES

Displacements	Constant accuracy	Calculated accuracy
ΔX (in m)	0.0135 ± 0.0081	0.0136 ± 0.0021
ΔY (in m)	-0.2964 ± 0.0077	-0.2963 ± 0.0046
ΔZ (in m)	0.0345 ± 0.0009	0.0342 ± 0.0009
ΔHz (in m)	0.2967 ± 0.0111	0.2966 ± 0.0051
ΔHz (fault par) (in m)	0.2959 ± 0.0108	0.2959 ± 0.0048
ΔHz (NLOD) (in m)	0.3094	0.3094
Runtime (in min)	6.1	71.4

TABLE VII

COMPARISON OF HORIZONTAL FAULT-PARALLEL ALS-MLS ESTIMATE TO NLOD ALINEMENT ARRAY STATION ESTIMATE FOR SEPTEMBER 2, 2014 MLS–SEPTEMBER 9, 2014 ALS FOR NAPA FAULT AT BROWNS VALLEY NEIGHBORHOOD WITH CONSTANT PA ESTIMATES AND TOTAL PA ESTIMATES

Displacements	Constant accuracy	Calculated accuracy
ΔX (in m)	0.0047 ± 0.0051	0.0047 ± 0.0012
ΔY (in m)	-0.0065 ± 0.0035	-0.0065 ± 0.0031
ΔZ (in m)	0.0060 ± 0.0019	0.0058 ± 0.0009
ΔHz (in m)	0.0080 ± 0.0062	0.0080 ± 0.0033
ΔHz (fault par) (in m)	0.0076 ± 0.0058	0.0076 ± 0.0029
ΔHz (NLOD) (in m)	0.0045	0.0045
Runtime (in min)	3.4	65.6

Our first analysis used the June 2014 ALS data set as pre-event and September 2 MLS as the postevent data set to derive displacements. The MLS points were conditioned to lie on the best fit ALS planes and the displacement results were provided in the first column of Table VI. The number of planes extracted as common surfaces in the ALS–MLS case was found to be less than both the ALS–ALS and MLS–MLS case due to difference in look angle of the airborne and mobile laser scanners; however, there was still a sufficient distribution of planar surfaces at varying look angles to provide a reliable solution. The fault parallel displacement estimate was compared to the NLOD estimated displacement during the same period. The result showed that the fault-parallel displacement agrees with the alinement array within the estimated accuracy of the ALS–MLS displacement. Variable PA estimates were also used to weight the displacement calculation (second column of Table VI). The variable PA provided values closer to the alinement array values while increasing the estimated accuracy of the recovered displacements.

The second ALS–MLS analysis used the September 2, 2014 MLS data set as the pre-event and the September 9, 2014 ALS data set as the postevent data set. The displacement results should provide the afterslip of the fault in the intervening period of 7 days. The results of the analysis with constant PA and with variable PA are provided in Table VII. The afterslip fault-parallel displacement result was again found to be very close to the estimated displacements from the alinement array. Including PA estimates into the solution increased the displacement accuracy estimates similar to previous results. The deviations between the ALS–MLS afterslip and the NLOD alinement station estimate were within the estimated accuracy of the ALS–MLS displacement estimates.

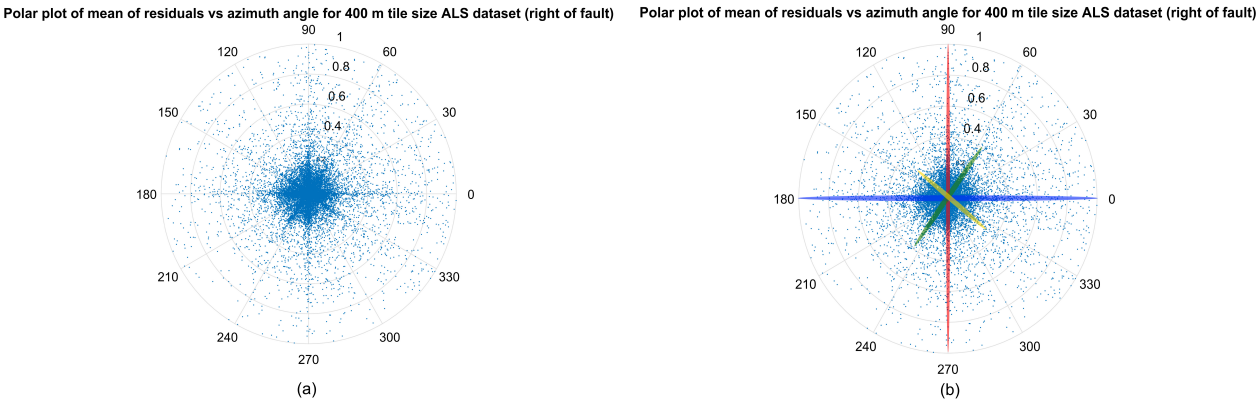

Fig. 10. (a) Polar plots of mean of residuals (in meters) versus azimuth angle (in degrees) for ALS data set east of fault trace with tile size 400 m. (b) Clusters for 400-m tiles shown in different colors with diametrically opposite clusters given same color.

TABLE VIII
COMPARISON OF HORIZONTAL FAULT-PARALLEL ALS-MLS ESTIMATE TO NLOD ALINEMENT ARRAY STATION ESTIMATE FOR SEPTEMBER 9, 2014 ALS–SEPTEMBER 30, 2014 MLS FOR NAPA FAULT AT BROWNS VALLEY NEIGHBORHOOD WITH CONSTANT PA ESTIMATES AND TOTAL PA ESTIMATES

Displacements	Constant accuracy	Calculated accuracy
ΔX (in m)	0.006 $\pm$ 0.0061	0.005 $\pm$ 0.0026
ΔY (in m)	-0.017 $\pm$ 0.0087	-0.017 $\pm$ 0.0039
ΔZ (in m)	0.0030 $\pm$ 0.0009	0.0026 $\pm$ 0.0009
ΔHz (in m)	0.0180 $\pm$ 0.0106	0.0178 $\pm$ 0.0047
ΔHz (fault par) (in m)	0.0176 $\pm$ 0.0102	0.0173 $\pm$ 0.0041
ΔHz (NLOD) (in m)	0.013	0.013
Runtime (in min)	3.4	79.1

The final analysis used the September 9 ALS data set as the pre-event and the September 30 MLS data set as the postevent data set to compute the displacements (Table VIII).

The results were consistent with the previous comparisons and showed that errors in horizontal fault-parallel displacements could be extracted at the subcentimeter level using ALS and MLS data sets.

C. South Rural Napa MLS Displacements

As previously mentioned, the southern portion of the Napa MLS data set is closer to the epicenter of the earthquake and had much smaller coseismic displacements but a higher observed and predicted afterslip; up to 30 cm over a 2–3 year period [11]. This region, shown in Fig. 2, consists of mostly ranch houses and has two alinement array stations set up near the study area, labeled as NLAR and NWIT. The region is an interesting test of our proposed methodology due to the sparseness of buildings (and therefore planes) that allowed us to examine the robustness of the algorithm. For the south rural areas, MLS data sets were captured on September 1, 2014 (t$-$1) and September 28 and 29, 2014 (t), data set of a 8 km2 area, as shown in the bottom black box of Fig. 2.

The same processing steps were applied to this data set as the previous MLS data sets. However, the plane extraction analysis was performed using 100-m segmented tiles for the entire data set for octree voxelization. This was a larger tile size than that used for the suburban Napa area; however, smaller tiles would not be useful due to the sparseness of man-made structures. The estimates of displacement, given in Table IX, showed that the afterslip was still predicted quite accurately, even with a sparse number of planar surfaces. The result agreed to 0.0003 m of the NLAR estimate, which was within the expected accuracy of the alinement array measurements and the estimated MLS displacement accuracy. The result was significantly less than the NWIT estimate (difference of 0.0037 m), but this might be because NWIT is slightly north of the study block and closer to the location of the expected maximum afterslip for the rupture. The inclusion of PA estimates did not change the displacement estimates appreciably but did increase the least squares confidence estimates for the computed MLS displacements.

TABLE IX
AFTERSLIP ESTIMATES FOR NAPA VALLEY FAULT AT SOUTH RURAL NAPA WITH CONSTANT PA ESTIMATES AND TOTAL PA ESTIMATES

Displacements	Constant accuracy	Calculated accuracy
ΔX (in m)	0.0105 $\pm$ 0.0027	0.0105 $\pm$ 0.0008
ΔY (in m)	-0.0623 $\pm$ 0.0047	-0.0621 $\pm$ 0.0009
ΔZ (in m)	0.0161 $\pm$ 0.0089	0.0161 $\pm$ 0.0009
ΔHz (in m)	0.0632 $\pm$ 0.0046	0.0632 $\pm$ 0.0073
ΔHz (fault par) (in m)	0.0583 $\pm$ 0.0042	0.0583 $\pm$ 0.0064
ΔHz (NLAR) (in m)	0.0580	0.0580
ΔHz (NWIT) (in m)	0.0622	0.0622
Runtime (in min)	7.8	36.7

V. COMPARISON OF THE DISPLACEMENT ERROR ESTIMATES

The displacement estimation process is a least squares adjustment and, therefore, can provide expected confidence levels in the displacement estimate. These errors will be reasonably and approximately sized if the accuracy of the individual observations (points) is well modeled and if there are no systemic errors in the observations. Table X quantifies the error of the fault-parallel displacements with respect to the alinement array and the least squares estimated displacement accuracy for all data sets analyzed. The initial analysis of the PA for MLS data sets assumed a constant noise variance in all three dimensions. This approach is suboptimal as it is apparent that the magnitude of noise is not constant but varies for each laser point. Thus, with the inclusion of PA estimation, the residual observational error should be Gaussian.

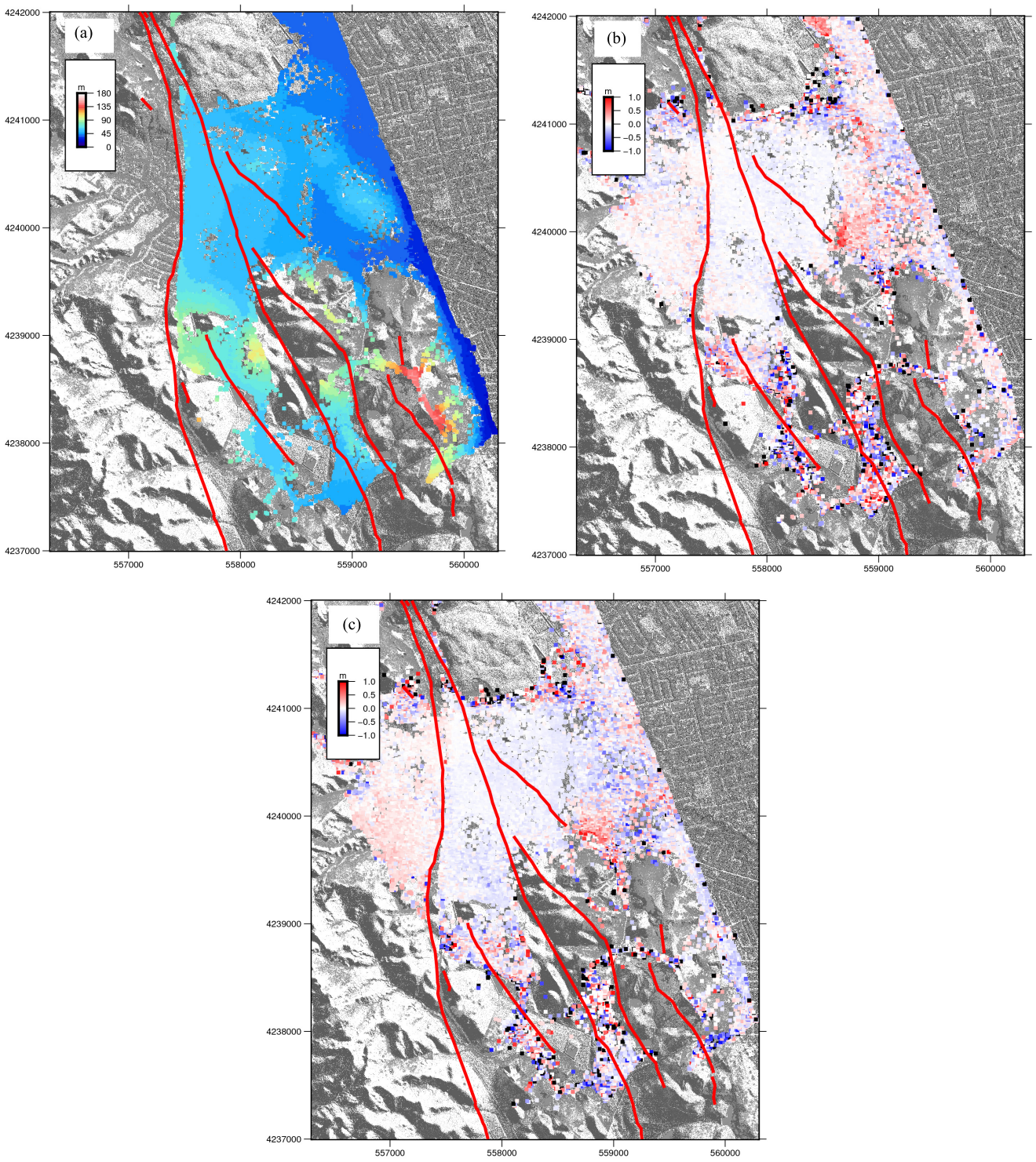

Fig. 11. (a) Spatial distribution of clusters from the polar plot for planes on the right side of fault trace. (b) Local X displacements found using 400 m × 400 m tile sizes with 20-m moving window size. (c) Local Y displacements found using 400 m × 400 m tile sizes with 20-m moving window size. Red solid line: fault traces.

It can be seen that the MLS displacements give estimates which are closest to the alinement array results. Another obvious conclusion that can be drawn from the table is that displacement accuracy estimates can be compared for the type of sensor used for data collection. Therefore, the MLS–MLS displacement analysis has the smallest accuracy values while ALS–ALS has the largest (in the centimeter level).

Although qualitative analysis has been provided for the displacement accuracy estimates, no quantitative measure has been shown to compare the size of the estimated accuracy for the displacement errors. A scale (relative magnitude) measure (ratio of the displacement error to the norm of displacement accuracy) is provided in the table to analyze whether the accuracy estimates are reasonable. The reasonability assertion

TABLE X

QUANTIFICATION OF DISPLACEMENT ERROR (Δdisplacement = $\Delta Hz_{\text{fault parallel}}$ - $\Delta Hz_{\text{alinement}}$) WITH RESPECT TO DISPLACEMENT ACCURACY ESTIMATES FOR DATA SETS WITH CONSTANT PA AND WITH ESTIMATED PA. RELATIVE MAGNITUDES PROVIDE THE CHANGE WITH RESPECT TO ESTIMATED ACCURACY FROM LEAST SQUARES. ESTIMATED VARIANCE FACTORS ARE PROVIDED FOR LEAST SQUARE ESTIMATES. J: JUNE DATA SET. S: SEPTEMBER DATA SET

Dataset	$\Delta displacement$ (ΔD) [m]	X accuracy (σ_X) [m]	Y accuracy (σ_Y) [m]	Z accuracy (σ_Z) [m]	Scale ($\frac{\Delta D}{\sqrt{\sigma_X^2+\sigma_Y^2+\sigma_Z^2}}$)	Variance (estimated) (left\right)	Relative scale ($\frac{\Delta D}{\sigma^2 * \sqrt{\sigma_X^2+\sigma_Y^2+\sigma_Z^2}}$)
Browns MLS-MLS	0.0015	0.0029	0.0054	0.0024	0.2358	1.6937\1.7499	0.1395
Browns MLS-MLS [PA]	0.0005	0.0011	0.0013	0.0009	0.2597	1.1944\1.3190	0.2081
Browns ALS-ALS	0.0043	0.0134	0.0159	0.0078	0.1349	1.4484\1.5708	0.1212
J ALS- 2nd S MLS	0.0131	0.0081	0.0077	0.0009	2.1759	2.1412\2.8682	0.4725
J ALS- 2nd S MLS [PA]	0.0131	0.0021	0.0046	0.0009	2.5506	2.8102\2.9890	0.8896
S 2nd ALS- S 9th MLS	0.0031	0.0051	0.0035	0.0019	0.4791	1.4871\1.3928	0.3427
S 2nd ALS- S 9th MLS [PA]	0.0031	0.0012	0.0031	0.0009	0.8141	1.4102\1.7805	0.5842
S 9th ALS- S 30th MLS	0.0046	0.0061	0.0087	0.0009	0.4314	1.2859\1.7174	0.2973
S 9th ALS- S 30th MLS [PA]	0.0044	0.0026	0.0039	0.0009	0.9638	1.3124\1.6128	0.6503
South Napa MLS-MLS	0.0003	0.0027	0.0047	0.0089	0.0288	0.777\0.9671	0.0738
South Napa MLS-MLS [PA]	0.0003	0.0008	0.0009	0.0009	0.0334	0.7989\0.9518	0.2884

provides that the norm of estimated accuracy should be in the range of 1 of the displacement errors (relative magnitude 0.68). If the scale is relatively large, then the norm of estimated accuracy is much smaller compared to displacement error, which shows that the accuracy estimates are not reasonable. Similarly, very small scale values indicate unreasonable accuracy estimates. However, the relative magnitudes of all data sets should also follow a normal distribution and, therefore, should have a mean of 0.68 ideally. The relative magnitudes for all data sets range between 0.01 and 2.55 with a mean of 0.6770 and standard deviation of 0.8469 showing that the algorithm can estimate the displacements accurately and robustly. The June ALS data set–September 2 MLS data set combination has a relative magnitude which is an order of magnitude higher than the others. Also, the displacements calculated with estimated PA can be shown to find relative magnitudes which are higher than those estimated using constant PA. That does show that inclusion of estimated PA enhances the quality of the least squares solution. This also shows that in the absence of ground truth, we can be confident that the least squares approach will give realistic estimates of accuracy, assuming there are no remaining systematic errors in the point cloud.

Finally, the reference or estimated variance factor σ^2, which includes the effect of all observation errors and determines the quality of least squares model, is reported in the Table X. The computed variance factor should ideally be close to 1 and a large deviation can be attributed to various factors as follows [42].

1) Undetected blunders in the observations.
2) The *a priori* estimates of the standard deviations are incorrect.
3) The constraints are tending to distort the adjustment.
4) Degrees of freedom are statistically small.

The estimated variance factors are calculated for the left and right sides separately to determine the quality of the least squares solution. We find that for all the displacement results, the estimated variance factors are close to 1, showing that the least squares solution has properly weighted observations.

Therefore from Table X, we can conclude that we can calculate displacements from MLS data sets at the millimeter level, from the ALS data sets at the 5-mm level and the combination of ALS–MLS data sets at the 3-mm level. This shows the viability of the use of the registration algorithm to estimate near-field subcentimeter-level displacements for earthquake deformation.

VI. CONCLUSION

An algorithm has been developed to automatically match planar surfaces and automate point-to-plane registration. The algorithms are applied to the problem of extraction of subcentimeter accuracy near-field earthquake deformation using MLS and ALS observed point clouds. The implementation of the planar growing steps was parallelized using GPGPU in OpenCL leading to a near real-time, robust, and precise segmentation algorithm. A planar least squares approach was detailed which performed a constrained solution to recover the transformation parameters by conditioning the points to lie on planar surfaces. The preprocessing steps for the least squares operation matched up planar surfaces from the temporally spaced point clouds. This was performed by finding the angle between the normals and the centroid-to-plane distance within certain tolerance thresholds. The least squares approach utilized a rigid body transformation equation to estimate the displacements.

The least squares approach required estimates of PA to derive the final displacement accuracy. The initial PA estimates were constant values derived from previous experience. The hardware error sources were determined from manufacturer specifications while the error due to scene geometry was estimated by estimating the ellipse formed by the intersection of the cone from the laser vector and the local best-fit plane. The total point uncertainty was the addition of the nominal error and the error due to the scene geometry. The PA estimation could then be used for deriving realistic estimates of displacements and associated estimated accuracy.

Various combinations of ALS and MLS data sets from the Napa fault were used to estimate fault surface displacements. Displacement estimates show that the least squares technique

can be used effectively for deriving fault-parallel surface displacements in the subcentimeter level without the presence of ground truth with high accuracy. This method can, therefore, provide very useful displacement estimates in earthquakes occurring in urban and semiurban areas having pre-event LiDAR data.

A possible limitation of our approach is that fault displacement is not the sole cause of apparent planar surface motion. It can also be caused by other phenomena, for example, rebuilding or renovation of structures between LiDAR acquisitions. Our future work will incorporate registration of natural surfaces (such as terrain) to determine offsets in rock outcrops and remote areas. Natural surfaces are difficult to quantify as parametric surfaces but can be approximated using an objective function which uses a higher order approximation for the samples of the surface. The problem can then be posed from a geometric optimization perspective to understand the underlying properties and lead to faster global and local convergence. Registration then can be formulated as a constrained non-linear least squares problem. Mitra *et al.* [43] use a squared distance function between the model and the data by approximating a quadratic surface for the data points. Adding to the former work, the study in [44] uses different registration formulations to minimize quadratic functions between model and data. Moving least squares has also been used in [45] to reconstruct surfaces from point cloud data which provides a good approximation of the point cloud data. These need to be evaluated for their suitability in estimating surface displacements. The authors believe that the existing framework can be easily modified to incorporate free-form surfaces to extract displacements from temporally spaced point clouds and it is hoped that the work can form the basis of earthquake deformation studies and provide greater understanding to the near-field displacement problem.

APPENDIX
SOLVING LEAST SQUARES EQUATIONS

Solving the functional model requires a generalized least squares (Gauss–Helmert) adjustment model, the work in [46] having two sets of unknowns, $\overrightarrow{x_1}$ and $\overrightarrow{x_2}$. The linearized form of the least squares equation is given as

$$A_1\hat{\delta}_1 + A_2\hat{\delta}_2 + B\hat{v} + w = 0 \tag{14}$$

where $A_1 = (\partial f/\partial x_1)$ and $A_2 = (\partial f/\partial x_2)$ are the respective design matrices of partial derivatives of the functional with respect to the unknowns; $B = (\partial f/\partial l)$ is the coefficient matrix of partial derivatives with respect to the observations; and $w = f(\overrightarrow{l}, \overrightarrow{x}^0)$ is the misclosure vector.

The planar constraint of the direction cosines having a unit length can be implemented as a constraint equation given as

$$a^2 + b^2 + c^2 - 1 = \hat{v_c} \tag{15}$$

which is a nonlinear equation. The equation is linearized similar to the previous equations as

$$G\delta_2 + w_c = v_c \tag{16}$$

where $G = (\partial g/\partial \overrightarrow{x_2})$ is the design matrix of partial derivatives with respect to the plane parameters; w_c is the constraint misclosure vector; and $\hat{v_c}$ is the constraint residual.

The stochastic model consists of a weight matrix P of weights for all the observations and a constraint weight matrix P_c having a fixed diagonal weight, as we assume all planes to be weighed equally.

The final normal equation form of the generalized least squares model is given as

$$\begin{bmatrix} A_1^T(BP^{-1}B^T)^{-1}A_1 & A_1^T(BP^{-1}B^T)^{-1}A_2 \\ A_2^T(BP^{-1}B^T)^{-1}A_1 & A_2^T(BP^{-1}B^T)^{-1}A_2 + G^T P_c G \end{bmatrix} \begin{bmatrix} \hat{\delta}_1 \\ \hat{\delta}_2 \end{bmatrix} + \begin{bmatrix} A_1^T(BP^{-1}B^T)^{-1}w \\ A_2^T(BP^{-1}B^T)^{-1}w + G^T P_c w_c \end{bmatrix} = \begin{bmatrix} 0 \\ 0 \end{bmatrix}. \tag{17}$$

ACKNOWLEDGMENT

Any use of trade, firm, or product names is for descriptive purposes only and does not imply endorsement by the U.S. Government.

REFERENCES

[1] D. M. Tralli, R. G. Blom, V. Zlotnicki, A. Donnellan, and D. L. Evans, "Satellite remote sensing of earthquake, volcano, flood, landslide and coastal inundation hazards," *ISPRS J. Photogramm. Remote Sens.*, vol. 59, no. 4, pp. 185–198, 2005.

[2] E. J. Fielding, T. J. Wright, J. Müller, B. E. Parsons, and R. Walker, "Aseismic deformation of a fold-and-thrust belt imaged by synthetic aperture radar interferometry near Shahdad, southeast Iran," *Geology*, vol. 32, no. 7, pp. 577–580, 2004.

[3] M. Matsuoka and F. Yamazaki, "Building damage mapping of the 2003 Bam, Iran, earthquake using Envisat/ASAR intensity imagery," *Earthquake Spectra*, vol. 21, no. S1, pp. 285–294, 2005.

[4] P. G. Somerville, "Magnitude scaling of the near fault rupture directivity pulse," *Phys. Earth Planet. Interiors*, vol. 137, nos. 1–4, pp. 201–212, 2003.

[5] D. Massonnet *et al.*, "The displacement field of the landers earthquake mapped by radar interferometry," *Nature*, vol. 364, no. 6433, pp. 138–142, 1993.

[6] D. T. Sandwell, L. Sichoix, D. Agnew, Y. Bock, and J.-B. Minster, "Near real-time radar interferometry of the Mw 7.1 Hector Mine Earthquak," *Geophys. Res. Lett.*, vol. 27, no. 19, pp. 3101–3104, 2000.

[7] R. Bürgmann, P. A. Rosen, and E. J. Fielding, "Synthetic aperture radar interferometry to measure Earth's surface topography and its deformation," *Annu. Rev. Earth Planet. Sci.*, vol. 28, no. 1, pp. 169–209, 2000.

[8] W. D. Barnhart *et al.*, "Geodetic constraints on the 2014 M 6.0 South Napa earthquake," *Seismol. Res. Lett.*, vol. 86, no. 2A, pp. 335–343, 2015.

[9] R. Michel, J.-P. Avouac, and J. Taboury, "Measuring near field coseismic displacements from SAR images: Application to the Landers earthquake," *Geophys. Res. Lett.*, vol. 26, no. 19, pp. 3017–3020, 1999.

[10] P. Segall and J. L. Davis, "GPS applications for geodynamics and earthquake studies," *Annu. Rev. Earth Planet. Sci.*, vol. 25, no. 1, pp. 301–336, 1997.

[11] K. W. Hudnut *et al.*, "Key recovery factors for the August 24, 2014, South Napa earthquake," U.S. Dept. Interior, U.S. Geol. Surv., Tech. Rep. 2014-1249, 2014, p. 51.

[12] S. Leprince, F. Ayoub, Y. Klinger, and J.-P. Avouac, "Co-registration of optically sensed images and correlation (COSI-Corr): An operational methodology for ground deformation measurements," in *Proc. IEEE Int. Geosci. Remote Sens. Symp. (IGARSS)*, Jul. 2007, pp. 1943–1946.

[13] C. W. D. Milliner, J. F. Dolan, J. Hollingsworth, S. Leprince, F. Ayoub, and C. G. Sammis, "Quantifying near-field and off-fault deformation patterns of the 1992 M_w 7.3 Landers earthquake," *Geochem., Geophys., Geosyst.*, vol. 16, no. 5, pp. 1577–1598, 2015.

[14] J.-P. Avouac *et al.*, "The 2013, M_w 7.7 Balochistan earthquake, energetic strike-slip reactivation of a thrust fault," *Earth Planet. Sci. Lett.*, vol. 391, pp. 128–134, Feb. 2014.

[15] K. Hudnut, A. Borsa, C. Glennie, and J.-B. Minster, "High-resolution topography along surface rupture of the 16 October 1999 Hector Mine, California, earthquake (M_w 7.1) from airborne laser swath mapping," *Bull. Seismol. Soc. Amer.*, vol. 92, no. 4, pp. 1570–1576, 2002.
[16] M. E. Oskin *et al.*, "Near-field deformation from the El Mayor–Cucapah earthquake revealed by differential LIDAR," *Science*, vol. 335, no. 6069, pp. 702–705, 2012.
[17] E. Nissen, A. K. Krishnan, J. R. Arrowsmith, and S. Saripalli, "Three-dimensional surface displacements and rotations from differencing pre- and post-earthquake LiDAR point clouds," *Geophys. Res. Lett.*, vol. 39, no. 16, pp. L16301-1–L16301-6, 2012.
[18] E. Nissen *et al.*, "Coseismic fault zone deformation revealed with differential lidar: Examples from Japanese Mw ~ 7 intraplate earthquakes," *Earth Planet. Sci. Lett.*, vol. 405, pp. 244–256, Aug. 2014.
[19] X. Zhang, C. Glennie, and A. Kusari, "Change detection from differential airborne LiDAR using a weighted anisotropic iterative closest point algorithm," *IEEE J. Sel. Topics Appl. Earth Observ. Remote Sens.*, vol. 8, no. 7, pp. 3338–3346, Jul. 2015.
[20] P. J. Besl and N. D. McKay, "Method for registration of 3-D shapes," *Proc. SPIE*, vol. 1611, pp. 586–607, Apr. 1992.
[21] K. Williams, M. J. Olsen, G. V. Roe, and C. Glennie, "Synthesis of transportation applications of mobile LiDAR," *Remote Sens.*, vol. 5, no. 9, pp. 4652–4692, 2013.
[22] B. T. Aagaard, J. J. Lienkaemper, and D. P. Schwartz, "Probabilistic estimates of surface coseismic slip and afterslip for hayward fault earthquakes," *Bull. Seismol. Soc. Amer.*, vol. 102, no. 3, pp. 961–979, 2012.
[23] K. Zhou, M. Gong, X. Huang, and B. Guo, "Data-parallel octrees for surface reconstruction," *IEEE Trans. Vis. Comput. Graphics*, vol. 17, no. 5, pp. 669–681, May 2011.
[24] J. E. Stone, D. Gohara, and G. Shi, "OpenCL: A parallel programming standard for heterogeneous computing systems," *Comput. Sci. Eng.*, vol. 12, no. 3, pp. 66–73, 2010.
[25] C. M. Shakarji, "Least-squares fitting algorithms of the NIST algorithm testing system," *J. Res. Nat. Inst. Standards Technol.*, vol. 103, no. 6, pp. 633–641, 1998.
[26] G. H. Golub and C. F. Van Loan, *Matrix Computations*. Baltimore, MD, USA: The Johns Hopkins Univ. Press, 1989.
[27] Y. Soh, H. Ashraf, Y. Hae, and I. Kim, "A hybrid approach to parallel connected component labeling using CUDA," *Int. J. Signal Process. Syst.*, vol. 1, no. 2, pp. 130–135, 2013.
[28] A. Kusari, "Precise registration of laser mapping data by planar feature extraction for deformation monitoring," Ph.D. dissertation, Dept. Civil Environ. Eng., Univ. Houston, Houston, TX, USA, 2015.
[29] J. Skaloud and D. Lichti, "Rigorous approach to bore-sight self-calibration in airborne laser scanning," *ISPRS J. Photogramm. Remote Sens.*, vol. 61, no. 1, pp. 47–59, Oct. 2006.
[30] K. W. Morin, "Calibration of airborne laser scanners," Dept. Geomatics Eng., Univ. Calgary, Calgary, AB, Canada, UCGE Rep. 20179, 2002.
[31] C. Glennie, "Rigorous 3D error analysis of kinematic scanning LIDAR systems," *J. Appl. Geodesy*, vol. 1, no. 3, pp. 147–157, 2007.
[32] P. Schaer, J. Skaloud, S. Landtwing, and K. Legat, "Accuracy estimation for laser point cloud including scanning geometry," in *Proc. Mobile Mapping Symp.*, Padova, Italy, 2007.
[33] J. Bray, J. Cohen-Waeber, T. Dawson, T. Kishida, and N. Sitar, "Geotechnical Engineering Reconnaissance of the August 24, 2014 M6 South Napa Earthquake," Geotech. Extreme Event Reconnaissance Assoc., GEER Rep. GEER-037, Jan. 2015.
[34] A. E. Morelan, C. C. Trexler, and M. E. Oskin, "Surface-rupture and slip observations on the day of the 24 August 2014 South Napa earthquake," *Seismol. Res. Lett.*, vol. 86, no. 4, pp. 1119–1127, 2015.
[35] S. Wei *et al.*, "The 2014 Mw 6.1 South Napa earthquake: A unilateral rupture with shallow asperity and rapid afterslip," *Seismol. Res. Lett.*, vol. 86, no. 2A, pp. 344–354, 2015.
[36] T. M. Brocher *et al.*, "The Mw 6.0 24 August 2014 South Napa earthquake," *Seismol. Res. Lett.*, vol. 86, no. 2A, pp. 309–326, 2015.
[37] B. A. Brooks *et al.*, "Buried shallow fault slip from the South Napa earthquake revealed by near-field geodesy," *Sci. Adv.*, vol. 3, no. 7, p. e1700525, 2017.
[38] J. J. Lienkaemper, S. B. DeLong, C. J. Domrose, and C. M. Rosa, "Afterslip behavior following the 2014 M 6.0 South Napa earthquake with implications for afterslip forecasting on other seismogenic faults," *Seismol. Res. Lett.*, vol. 87, no. 3, pp. 609–619, 2016.
[39] X. Meng, N. Currit, and K. Zhao, "Ground filtering algorithms for airborne LiDAR data: A review of critical issues," *Remote Sens.*, vol. 2, no. 3, pp. 833–860, 2010.
[40] P. Axelsson, "DEM generation from laser scanner data using adaptive TIN models," *Int. Arch. Photogramm. Remote Sens.*, vol. 33, pp. 111–118, Jan. 2000.
[41] J. Boatwright, K. E. Budding, and R. V. Sharp, "Inverting measurements of surface slip on the Superstition Hills fault," *Bull. Seismol. Soc. Amer.*, vol. 79, no. 2, pp. 411–423, 1989.
[42] N. Lin, V. Kidd, S. Moon, and G. Hilley, "Tracking the San Andreas fault in northern California using Airborne Laser Swath Mapping Data," in *AGU Fall Meeting Abstr.*, 2010.
[43] N. J. Mitra, N. Gelfand, H. Pottmann, and L. Guibas, "Registration of point cloud data from a geometric optimization perspective," in *Proc. Eurograph./ACM SIGGRAPH Symp. Geometry Process.*, 2004, pp. 22–31.
[44] H. Pottmann, Q.-X. Huang, Y.-L. Yang, and S.-M. Hu, "Geometry and convergence analysis of algorithms for registration of 3D shapes," *Int. J. Comput. Vis.*, vol. 67, no. 3, pp. 277–296, 2006.
[45] R. Kolluri, "Provably good moving least squares," *ACM Trans. Algorithms*, vol. 4, no. 2, p. 18, 2008.
[46] E. M. Mikhail and F. E. Ackermann, *Observations and Least Squares*. 1976.

Arpan Kusari (M'18) received the M.S. degree in geomatics engineering from Purdue University, West Lafayette, IN, USA, in 2011, and the Ph.D. degree in civil engineering, with a major in geosensing concentration, from the University of Houston, Houston, TX, USA, in 2015.

He is currently a Research Scientist with Ford Motor Company, where he is involved in sensor localization, dynamic obstacle tracking, and decision making of autonomous vehicles.

Craig L. Glennie (M'12) the received the B.Sc. and Ph.D. degrees in geomatics engineering from the University of Calgary, Calgary, AB, Canada, in 1996 and 1999, respectively.

He was the Vice President of Engineering with Terrapoint, Houston, TX, USA. He is currently an Associate Professor of civil and environmental engineering with the University of Houston, Houston, TX, USA, a Registered Professional Engineer in Alberta, and a Co-Principal Investigator with the NSF-funded National Center for Airborne Laser Mapping, Houston, TX, USA. His research interests include the design, development, and operation of kinematic remote sensing systems.

Benjamin A. Brooks (M'18) received the B.Sc. degree from the University of California at Santa Cruz, Santa Cruz, USA, in 1991, and the Ph.D. degree from Cornell University, Ithaca, NY, USA, in 1999.

He was the Director of the Pacific GPS Facility, University of Hawai'i, Honolulu, HI, USA. He is currently a Research Geophysicist with the United States Geological Survey, Earthquake Science Center, Menlo Park, CA, USA. His research interests include all aspects of earthquake geodesy, especially near-field high-resolution measurements.

Todd L. Ericksen received the B.Sc. degree from Texas A& M University College Station, TX, USA, in 1994, and the M.Sc. degree from the University of Hawai'i at Manoa, Honolulu, HI, USA, in 1998.

He is currently a Licensed PE with Civil Branch, HI, USA, with a background in remote sensing and instrumentation and a Geodesist with the United States Geological Survey, Earthquake Science Center, Menlo Park, CA, USA. His research interests include mobile LiDAR applications, low-cost sensors, and seafloor geodesy.